BioImage Informatics

A Principal Skeleton Algorithm for Standardizing Confocal Images of Fruit Fly Nervous Systems

Lei Qu[1,2], and Hanchuan Peng[1,2,*]

[1]Janelia Farm Research Campus, Howard Hughes Medical Institute, Ashburn, VA, 20147.

[2] Equal contribution.

[*] Corresponding author, pengh@janelia.hhmi.org

ABSTRACT

Motivation:

The fruit fly (*Drosophila melanogaster*) is a commonly used model organism in biology. We are currently building a 3D digital atlas of the fruit fly larval nervous system based on a large collection of fly larva GAL4 lines, each of which targets a subset of neurons. To achieve such a goal, we need to automatically align a number of high-resolution confocal image stacks of these GAL4 lines. One commonly employed strategy in image pattern registration is to first globally align images using an affine transform, followed by local nonlinear warping. Unfortunately, the spatially articulated and often twisted larval nervous system makes it difficult to globally align the images directly using the affine method. In a parallel project to build a 3D digital map of the adult fly ventral nerve cord, we are confronted with a similar problem.

Results: We proposed to standardize a larval image by best aligning its principal skeleton (PS), and thus used this method as an alternative of the usually considered affine alignment. The principal skeleton of a shape was defined as a series of connected polylines that spans the entire shape as broadly as possible, but with the shortest overall length. We developed an automatic principal skeleton detection algorithm to robustly detect the principal skeleton from an image. Then for a pair of larval images, we designed an automatic image registration method to align their principal skeletons and the entire images simultaneously. Our experimental results on both simulated images and real datasets showed that our method does not only produce satisfactory results for real confocal larval images, but also perform robustly and consistently when there is a lot of noise in the data. We also applied this method successfully to confocal images of some other patterns like the adult fruit fly ventral nerve cord and center brain, which have more complicated principal skeleton. This demonstrates the flexibility and extensibility of our method.

Availability: The supplementary movies, full size figures, test data, software, and tutorial on the software can be downloaded freely from our website http://penglab.janelia.org/proj/principal_skeleton.

1 INTRODUCTION

The fruit fly (*Drosophila melanogaster*) is one of most studied model organisms in biology. It is currently used widely to under-stand how a real nervous system works. A systems biology approach we are taking to study the fruit fly brain is to produce 3D digital atlases of this animal's nervous system at various developmental time points, including adult, larval and embryonic stages. We have been taking advantage of an on-going effort to generate a collection of 8,000 enhancer-trap GAL4 lines that would have their neuronal patterns cover the entire set of neurons in the fruit fly nervous system (Pfeiffer, et al, 2008). High-resolution 3D confocal images of these GAL4 lines were produced. The scale of the problem is large, in terms of both the large-size of each 3D confocal image (hundreds of megabytes to multi-gigabytes each) and the large-number of the images in the database (2 to 5 times of the number of GAL4 lines, as multiple flies of the same GAL4 line need to be imaged). Therefore, an informatics challenge is how to map the neuronal patterns onto a "standard" brain in an accurate, reliable, and automatic way.

A brain mapping study needs several enabling techniques, including 3D image registration (alignment), neurite tracing, neuronal pattern classification, visualization, and mining methods (Peng, 2008). It is often critical to align image patterns that have various orientations, sizes, shape deformations, and intensity changes. A classic routine for 3D image pattern registration is to first align patterns globally, followed by a local alignment to transform one pattern to the other (Rueckert et al, 1999; Toga, 1999). For a pair of image patterns, the purpose of the global alignment is to standardize the patterns as a whole so that they possess similar scales, positions and directions. The affine transformation is commonly used for global alignment. Once two patterns have been roughly aligned globally, it is much easier to use the more sophisticated local alignment (e.g. Rueckert, et al, 1999; Sorzano, et al, 2005), which is often nonlinear and deformable, to register the patterns precisely. The affine alignment was already successfully used in recent efforts to build digitized atlases for model animals, such as the Allen mouse brain atlas (Lein, et al, 2007), the adult fruit fly brain atlas (unpublished work of Peng lab), and the single-nucleus resolution atlas of the nematode *C. elegans* (Long, et al, 2009).

However, for the alignment problem of the fruit fly larval nervous system (LNS) in this paper, we found that the global affine alignment can hardly be used. As shown in Fig. 1a, in the LNS the

two brain hemispheres and the ventral nerve cord (VNC) form an articulated structure, which is flexible and often skews toward one side. This deformation cannot be described using global rotation, translation, scaling and shear as used in the affine transform. Fig. 1c, which is an example of the adult VNC, displays a similar deformation of the shape. Therefore, we need a more sophisticated global alignment method to standardize the shape of these patterns, before we can proceed further to the local alignment.

Intuitively, we considered aligning the "backbone", or "midline", of a curved fruit fly LNS or an adult VNC (red skeletons in Fig. 1). A related study was to straighten the strongly curved body of *C. elegans* (Peng, et al, 2008) by first detecting the curved anterior-posterior axis of a worm, and then re-stacking the resampled image data on the entire series of 1-pixel spacing cutting-planes orthogonal to such a detected "backbone". This earlier method is very efficient for *C. elegans* confocal images and other similar cases where the backbone is a simple smooth curve, and the body of the pattern is not fat (wide) enough so that the slightly non-parallel cutting planes next to each other will not intersect within the pattern. Unfortunately, this method cannot be directly used in standardizing a fruit fly larval pattern because the articulated pattern cannot be described as a simple curve, and the fruit fly patterns are often fat/wide enough so that restacking the cutting planes may introduce artifacts especially in the articulated image regions. There are several other skeleton extraction methods (Lam, et al, 1992; Brandt, et al, 1992; Malandain, et al, 1998; Chuang, et al, 2004). However they cannot easily produce skeletons of the same topological structure for different input images, and thus will not be very useful for the registration.

Therefore, in this work we proposed a new approach to standardize the confocal images of fruit fly LNS and adult VNC. We detected the principal skeleton (PS) of a shape using an automatic skeleton deformation algorithm (Section 2). Then we designed a smooth warping method to best align the principal skeleton of a pair of image patterns (Section 3). Our method introduces a minimum amount of degradation of the image quality during the standardization. It is also robust under a variety of conditions. In addition, our method is general. It is not limited to fly larval patterns; indeed it can be applied to any image patterns that have a reasonable principal skeleton[1] (Section 4).

2 DETECTING PRINCIPAL SKELETON

Intuitively, the principal skeleton of a shape can be understood as its "backbone", which describes the basic structure as well as the major deformation of this shape. In this paper, we define the principal skeleton as a set of connected polylines that that spans the entire shape as broadly as possible and at the same time has the shortest overall length and sufficient smoothness. We call each polyline a segment. Each segment consists of multiple ordered control points.

Let us use the LNS (Fig. 1a) as an example. We view the nervous system as an articulated composition of three main parts: VNC, and left and right brain hemispheres. Despite the complexity in the articulation region, the deformation within each part can be approximated using a gentler curve. We define the principal skele-

ton of the LNS as a structure with 6 segments, including 3 branching segments, which represent the VNC, and left and right hemispheres respectively, jointed to another 3 segments of a triangle that models the "hole" where the non-neuronal tissues (gut and heart) pass through the articulation area.

Naturally, the principal skeleton can be viewed as a conceptual extension of the simple "backbone" curve of a *C. elegans* body (Peng, et al, 2008), which is essentially the principal curve (Hastie, 1994) of a distribution of image pixels. However, the principal skeleton is more than a simple collection of multiple principal curves due to the connection of segments. In addition, instead of using a smooth curve to model each skeleton segment, without loss of generality, we model them by polylines. The control points in a polyline can be further used to fit a smooth cubic-spline curve (Bartels, et al, 1998), similar to the *C. elegans* case.

Similar to the case of LNS, the principal skeleton of a fruit fly adult VNC can be defined as an ¥-shape (Fig. 1c). The same algorithm is used to find the principal skeletons for both cases. Throughout this manuscript, we focus on LNS; experimental results on adult VNC and some other cases will be presented at the end of this paper, and the corresponding movies can be found in the Supplements.
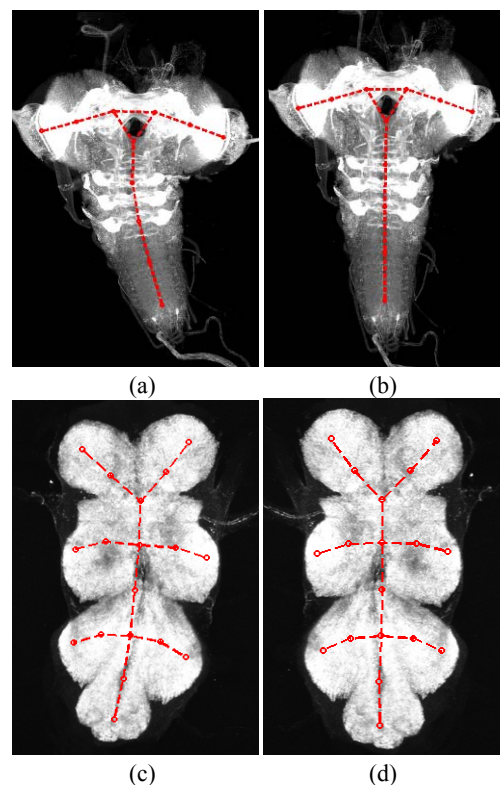

Fig. 1. Original and standardized fruit fly larva (a)(b) and adult VNC images (c)(d) along with their principal skeletons (dotted polylines).

2.1 Shape prior of larval principal skeleton

The shape prior defines the initial principal skeleton including its topology and constraints of its segments and control points. It should be as simple as possible but complicated enough to capture the major topology of the shape. During the optimization to be

---

[1] Some image patterns may not have a uniquely well-defined principal skeleton, such as a spherical cell that has the uniform intensity.

2

described below, the topology of a principal skeleton remains unchanged; however the locations of all segment-control points will be iteratively updated.

The shape prior of LNS is defined in Fig. 2. It contains totally 11 control points $c_1, \ldots, c_{11}$, which are arranged as 6 segments $B_1, \ldots, B_6$ in Eq. (1). The control points c_3, c_4, and c_7 join these 6 segments.

$$\begin{cases} B_1 = \{c_1, c_2, c_3\} \\ B_2 = \{c_4, c_5, c_6\} \\ B_3 = \{c_7, c_8, c_9, c_{10}, c_{11}\} \\ B_4 = \{c_3, c_4\} \\ B_5 = \{c_3, c_7\} \\ B_6 = \{c_4, c_7\} \end{cases} \quad (1)$$

We minimize the length of each segment. Sometimes we may need to minimize the overall length of multiple segments, which is indeed has a similar effect to maximizing the total smoothness of these segments when their length is short enough. For example, for the LNS, we would like to produce a very smooth skeleton for the junction area of the two brain hemispheres, which contains 3 segments B_1, B_4, and B_2. This is similar to forcing B_1, B_4, and B_2 to line up in an almost straight line, thus their total length is as short as possible. To attain this goal, in Eq. (2) we define 4 optimization "domains" $D_1, \ldots, D_4$, each of which is a polyline and may cover multiple segments (e.g. D_1).

$$\begin{cases} D_1 = B_1 \cup B_4 \cup B_2 = \{c_1, c_2, c_3, c_4, c_5, c_6\} \\ D_2 = B_3 = \{c_7, c_8, c_9, c_{10}, c_{11}\} \\ D_3 = B_5 = \{c_3, c_7\} \\ D_4 = B_6 = \{c_4, c_7\} \end{cases} \quad (2)$$
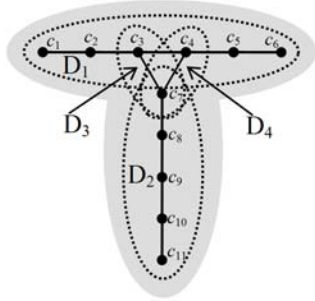

Fig. 2. The shape prior of the fruit fly larva principal skeleton, where 11 control points $c_1, \ldots, c_{11}$ form 6 connected segments and 4 domains. The domains, indicated by dotted eclipses, are used for the length constraint.

2.2 Energy minimizing deformable principal skeleton model

We design a deformable model to detect the principal skeleton, given its shape prior. We formulate an energy function consisting of an external energy term and an internal energy term. The external term is based on the image information, thus also called the "image term", to force the principal skeleton spanning as broadly as possible to cover an entire LNS. The internal term is based on the topology and constraints of skeleton domains; this term is

minimized to guarantee the least total length and maximum smoothness of the skeleton.

Let p denote an image pixel, W the image area and Ω the set of all control points of skeleton. The Voronoi region $\Theta(c_i)$ of the control point c_i is defined as the set of pixels in W that are closer to c_i than to any other control points:

$$\Theta(c_i) = \left\{ p \in W : \forall c_j \in \Omega, \|c_i - p\| \le \|c_j - p\| \right\} \quad (3)$$

We define the external term $E_{external}$ as:

$$E_{external} = \sum_{c_i \in \Omega} \|c_i - O(\Theta(c_i))\|^2, \quad (4)$$

where $O(\Theta)$ denotes the center of mass of a Voronoi region Θ.

We define the internal energy term by aggregating all optimization domains defined in Eq. (2). Since there are only a few control points in each domain (e.g. 5 in D_2 and 6 in D_1), minimizing their length has a comparable effect to smoothing. For simplicity, we only aggregate the length energy of each domain in the internal term. Let $U = \{D_1, D_2, D_3, D_4\}$ be the set of domain, we have:

$$E_{internal} = \frac{1}{\sum_{D_k \in U} w(D_k)} \sum_{D_k \in U} w(D_k) E_{length}(D_k), \quad (5)$$

where $w(D_k)$ is a coefficient that defines the contribution of domain D_k. For LNS, due to the vertical asymmetry of the shape prior, in order to avoid point c_3 and c_4 will be pulled downwards seriously by D_3 and D_4, we give D_1 more weight ($w(D_1)=10$, all other weights equal 1). For a general case, the weights can be uniform. $E_{length}(D_k)$ in Eq. (6) denotes the length of domain D_k:

$$E_{length}(D) = \sum_{n=1}^{|D|-1} \|D[n] - D[n+1]\|^2, \quad (6)$$

where $D[n]$ is the n-th element (control point) in domain D.

The overall energy E takes the form:

$$E = \alpha E_{external} + \beta E_{internal}, \quad (7)$$

where α and β are two positive coefficients (both equal 0.5 in our experiments).

To minimize Eq. (7) we solve the following equation for every c_i, $i=1,\ldots 11$:

$$\frac{\partial E}{\partial c_i} = \alpha \frac{\partial E_{external}}{\partial c_i} + \beta \frac{\partial E_{internal}}{\partial c_i} = 0. \quad (8)$$

It is easy to derive from Eq. (8) an iterative optimization method to estimate the new location of each non-tip control point, c_i^{t+1}, based on the Voronoi region's center of mass of its current position c_i^t, and the positions of its connected neighbor control points:

$$c_i^{t+1} = \frac{\alpha O(\Theta(c_i^t)) + \beta \frac{1}{N(c_i^t)} \sum_{D_k \in U, \, c_i^t \in D_k} w(D_k) \sum_{c_j \in P(D_k, c_i^t)} c_j^t}{\alpha + \beta \frac{1}{N(c_i^t)} \sum_{D_k \in U, \, c_i^t \in D_k} w(D_k) |P(D_k, c_i^t)|}, \quad (9)$$

where $N(c_i) = \sum_{D_k \in U, c_i \in D_k} w(D_k)$, and $P(D,c_i)$ denotes the set of neighboring control points of c_i in domain D (in our case, since each domain is a polyline, this set includes both the left and right control points of c_i). Note that $P(D,c_i)$ is null if $c_i \notin D$.

For the end points of the principal skeleton, i.e. c_1, c_6 and c_{11}, we use an empirically more robust formula based on the respective two neighboring control points. Let us use c_1 as an example, the simplified formula is:

$$c_1^{t+1} = \frac{\alpha O(\Theta(c_1^t)) + \beta(2c_2^t - c_3^t)}{\alpha + \beta} \qquad (10)$$

Other end points can be updated similarly. Normally, the algorithm converges within 100 loops.

We have implemented the principal skeleton detection method as a plugin of the V3D software (http://penglab.janelia.org/proj/v3d) (Peng, et al, 2010). We provide a tutorial in the Supplements on how to use the program.

3 ALIGNING PRINCIPAL SKELETONS

Since the principal skeleton of a fly LNS has a more complicated topology than the simple curved "backbone" of nematode *C. elegans*, we cannot simply reuse the cutting-plane re-stacking strategy in the earlier work (Peng *et al*, 2008) to standardize an LNS image. Instead, we generate a smooth displacement field (DF) to warp the fly larvae from one to another, based on their principal skeleton information.

There are three general requirements of a DF. (i) No singularity. Thus the DF should be smooth everywhere. (ii) There should be a minimum amount of distortion to geometrically warp the principal skeleton, as well as the entire LNS. (iii) The algorithm should be extensible to other principal skeletons; at the same time, when a principal skeleton consists of only one segment, the standardization should approximate the cutting-plane re-stacking method.

We produce a DF using thin plate spline (TPS) (Bookstein, 1989), which is defined as the least-bending smooth surface spanning a set of anchor points. Thus the requirements (i) and (ii) are met naturally. For requirement (iii), we first consider all control points of the principal skeleton as TPS anchor points. Then we use cubic-spline to find a smooth curve through each domain of the principal skeleton (as shown in Fig. 3(a)), and then for every consecutive pair of control points we add the halfway point on the smooth curve as a TPS anchor point. We call the set of anchor points that consists of nicely spaced points on the principal skeleton the PS-set. Next, we define additional anchor points based on this PS-set: for each PS-set anchor point, we compute the orthogonal cutting line that intersects at this anchor point location with the respective smooth curve in the principal skeleton, and then we define two anchor points on each of the left and right sides of the cutting line (spacing = 75 pixels for LNS). We call the set of anchor points that are not on the principal skeleton the non-PS-set. If a non-PS-set anchor point falls into the intersection region of multiple cutting lines of different domains (as highlighted in Fig. 3(a)), we remove it from the set of the all anchor points, and thus avoid the non-smooth wrapping-around of the displacement field.

While the choices of the number of anchor points of both PS-set and non-PS-set, as well as the spacing among anchoring points, are

empirical, a general guideline is to make the anchoring points distribute evenly to cover the entire image pattern. The selected parameters are then used for all images.

The entire algorithm for LNS-standardization is as following:
(1) Define/initialize the shape prior of the principal skeleton.
(2) Find the Voronoi region of each control point in an input image (called "subject" image below for simplicity).
(3) Update the positions of control points using Eqs. (9) and (10).
(4) Check whether or not the positions of control points have converged (i.e. the maximal distance between the new positions and old positions of control points is less than 0.01). If yes, go to step 5. Otherwise go back to step 2.
(5) Use cubic-spline to interpolate the principal skeleton and produce a smooth skeleton according to the defined domains.
(6) Define both the PS-set and non-PS-set of TPS anchor points, remove some non-PS-set points if they fall into the cutting line overlapping/intersection region.
(7) Compute the TPS DF of this image using the corresponding anchor points between this image and a predefined target image.
(8) Warp the subject image to a "standard" shape using the DF.
(9) Set the warped (standardized) subject image as the input image and repeat steps 1-8 until the principal skeleton of the image does not vary significantly (defined as the maximum displacement of control points between two consequent iterations less than 1 pixel).
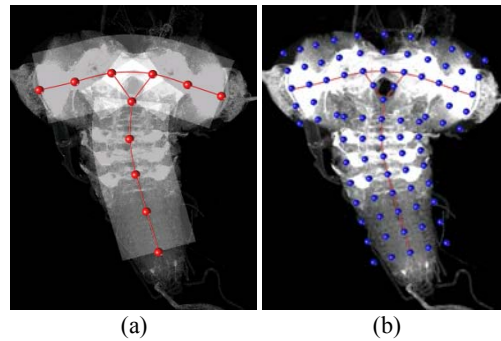

(a)   (b)

Fig. 3. Anchor points definition. (a) The curve is the cubic-spline smoothed PS; the surrounded gray masks illustrate where cutting lines may take place; the overlapped/highlighted mask region in the center of hemisphere indicates where the cutting lines of different domains may intersect. (b) Defined anchor points overlaid on the PS.

Our standardization method is general; it can be applied to both 2D and 3D image patterns. For fruit fly LNS, although our image stacks are 3D, the major variation of the shape is in the 2D plane of two brain hemispheres and the ventral nerve cord. Therefore, we simplify the processing using 2D maximum intensity projection, and detect the principal skeleton in 2D. Accordingly, the TPS DF is produced in 2D; all z-sections of a fly LNS image stack will share the same DF.

Of note, in our algorithm it is necessary to consider step 9, i.e. the iterative alignment of a principal skeleton. Because TPS warping is nonlinear and will cause some regions expand or shrink smoothly, the redetected principal skeleton of a warped image is slightly different from that of target image. Several iterations of the optimization will produce nicely aligned image patterns whose principal skeletons match well. Normally it takes about 3 loops to generate satisfactorily aligned principal skeletons (Section 4.4).

4 EXPERIMENTS AND DISCUSSION

We first evaluated the robustness and consistency of the principal skeleton detection algorithm, and then compared our method to the commonly used morphological thinning and affine-transform based alignment method. In the end, we show some principal skeleton detection results of other cases.

For the fruit fly larva data, N-cadherin labeled LNS was imaged in 3D using a confocal laser scanning microscope (Zeiss LSM 510) in the lab of J. Truman. The voxel resolution is 0.46×0.46×2.0 μm. For the adult fly VNC data, NC labeled VNC was imaged using a confocal microscope (Zeiss LSM Pascal 5) in J. Simpson's lab. The voxel resolution is 0.58×0.58×0.8 μm in 3D.
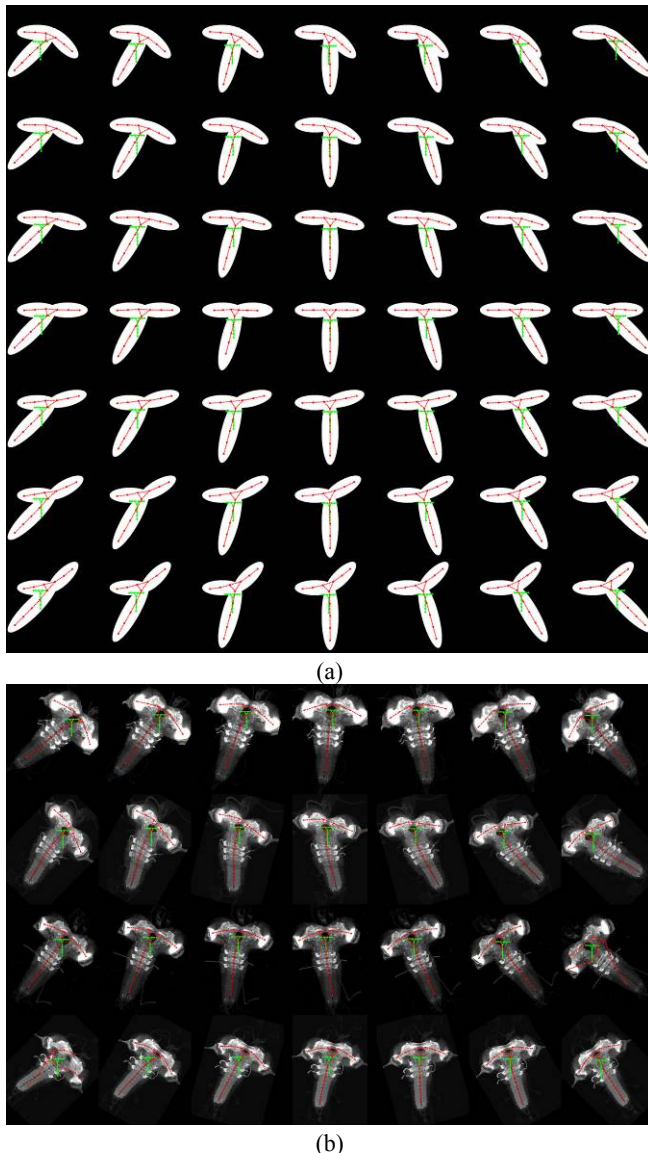

(a)

(b)

Fig. 4. Robustness evaluation using (a) different simulated twisted LNS and (b) different larva orientations. Green: initialization. Red: detected PS.

4.1 Robustness

We tested the robustness of detecting the principal skeleton when the LNS patterns in images have different orientations, scales, contrasts, articulated, and twisted parts, as well as other noises.

Fig. 4 (a) shows robustness test results for the twisted LNS. We simulated the deformation by rotating the right brain hemisphere from -45 to 45 degrees, with a 15-degree interval, to produce 7 rows from top to bottom. For every row, we rotated the VNC from -45 to 45 degrees similarly to produce 7 columns. The detected principal skeletons (red) from the same initialization (green) are correct, indicating that our method is robust for twisted patterns. We further added noise to the test images and changed the scale of the initialization. The results (in Supplements) were also robust.

Fig. 4 (b) shows a perturbation test based on real LNS images. We randomly selected four LNS images that have differently twisted nervous systems. Similarly to Fig. 4 (a), we rotated them with different angles (-45, -30, -15, 0, 15, 30 and 45 degrees). From exactly the same initialization (green), our algorithm successfully detected the principal skeletons (red), except two errors in the left-bottom corner and in the last column of the third row, which correspond to -45 degree and +45 degree rotation, respectively. The errors occurred when the angle between the longest axis (along the brain-VNC direction) of an LNS and the initialization of the principal skeleton is bigger than 45 degrees, the VNC part of the larva would more likely be interpreted as B_1 or B_2 rather than B_3 according to the shape prior we assumed in section 2. In other words, the principal skeleton was initialized too poorly. However, practically speaking, this situation is rare in the real data. We can also avoid it completely by preprocessing an image so that its longest axis is roughly aligned with the B_3 segment. We also changed the contrast of the test images and found that our method robustly produced meaningful results (see Supplements).

4.2 Consistency

We quantified the consistency of principal skeleton detection given different initializations. For four LNS images, we rotated the respective initial shape prior of the principal skeleton in the range of ±30 degrees (interval=15 degrees). For any pair of the five principal skeletons detected for each image, we computed the mean-square error (MSE) of the corresponding control points of this pair of skeletons. Table 1 shows the maximal and average MSE scores for all possible pairs. The MSE scores are much smaller than one pixel, indicating that principal skeletons were detected very consistently from different initializations.

Table 1. Consistency of principal skeleton detection under different initializations. The images 1~4 correspond to the middle column of Fig. 4(b).

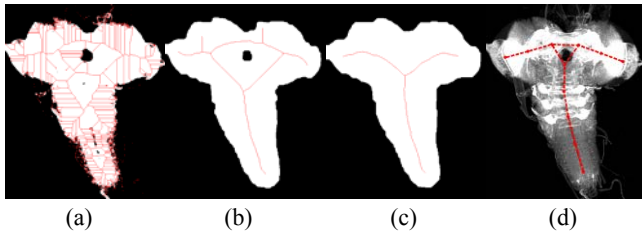| Image Score	Maximal MSE (pixel)	Average MSE (pixel)
1	0.035553	0.016931
2	0.047522	0.027183
3	0.003256	0.001953
4	0.027412	0.016448

Fig. 5. Skeletons detected using image thinning (a)(b)(c) under different conditions and using the principal skeleton method (d).
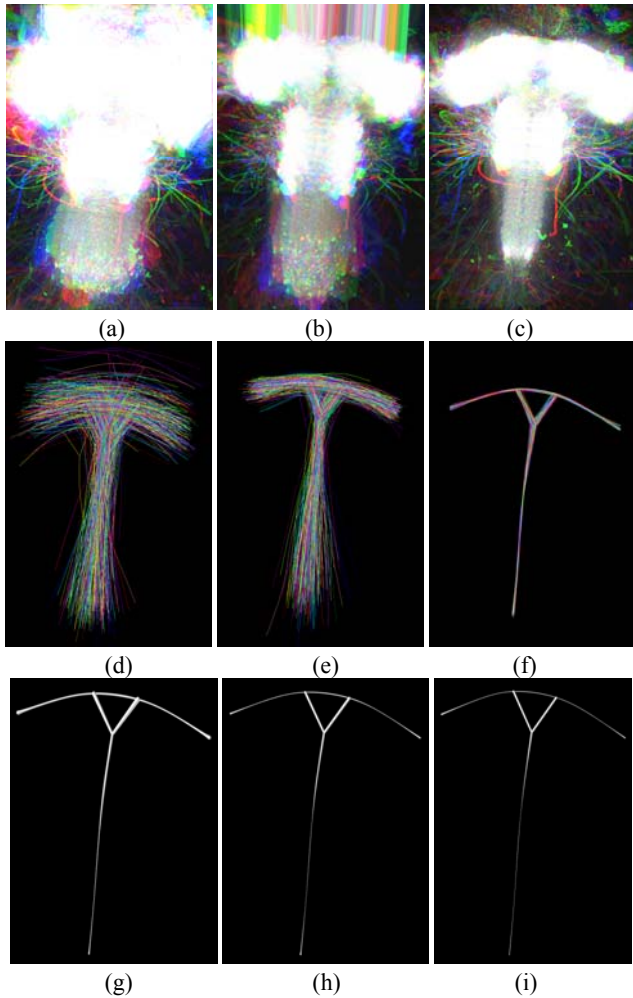

Fig. 6. Comparison of LNS standardization using the principal skeleton method and the affine-based alignment. ((a)~(c)), as well as the respective principal skeletons ((d)~(f)): before standardization ((a) and (d)), after a global alignment using affine transformation ((b) and (e)), and after our principal skeleton based warping method ((c) and (f)). The skeletons are periodically colored with 8 different colors, and the images are periodically colored with 3 colors (red, green and blue). (g)(h)(i) The density map of overlaid principal skeletons after 1, 2 and 3 iterations of optimization. The radius of skeleton indicates the standard deviation of principal skeletons of images after 1, 2 and 3 iterations of standardization.
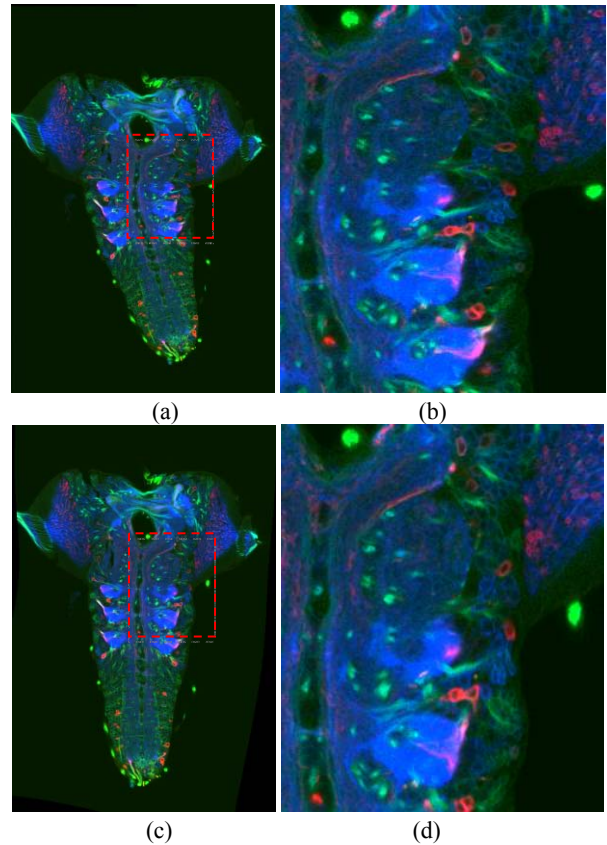

Fig. 7. Comparison of the image content before ((a)(b)) and after ((c)(d)) standardization. (d)(d) are the zoom-in view of the red boxes in (a)(c). Red image channel: GFP-tagged GAL4 patterns. Green: Neurotactin. Blue channel: N-cadherin.

4.3 Comparison with morphology thinning

Morphology thinning (Lam, et al, 1992) is a commonly used algorithm to extract the "backbone" of an image object that has closed contour. In order to use thinning, one needs to first segment the object from the image background. Unfortunately, the thinning algorithm is very sensitive to the segmentation. As shown in Fig. 5 (a), direct thinning on a binary image generated too many artificial branches due to spurs in the contour of the object and unstained areas (holes). Here we simply took the foreground as the set of the pixels whose intensity was above the mean value of all pixels in the image. After we carefully smoothed the contour and filled the holes using additional morphological opening and closing operations (with morphological element set to be "disk" shape, with 10 and 20 pixels in diameter, respectively), we achieved better thinning results in Fig. 5 (b) and (c), which however were still not as good as the detected principal skeleton in Fig. 5 (d).

4.4 Standardization of real LNS images

As a real application, we used the principal skeleton method to standardize a randomly selected set of 237 3D confocal images of the third instar larval stage LNS. Fig. 6 shows the comparison results of overlaid patterns ((a)~(c)), as well as the respective principal skeletons ((d)~(f)), before and after standardization. Obviously, the affine transform based standardization (Fig. 6 (b) and (e)) did not align LNS patterns well, especially the big deviation in

the VNC of an LNS. This was due to that the articulated LNS could not be well approximated by an affine transformation. On the contrary, the principal skeleton based standardization scheme (Fig. 6 (c) and (f)) successfully registered all images, with the principal skeletons almost exactly overlapping on top of each other.

We also quantified the spatial variations of the aligned principal skeletons. As explained at the end of Section 3, the iterative optimization of the principal skeleton standardization, i.e. step 9, is important. Fig. 6 (g), (h), and (i) show that with 1, 2, and 3 iterations, the standard deviation of the entire set of principal skeletons became smaller and smaller. Indeed, the average "pair-wise distance" of the entire population of principal skeletons dropped from 50.225 pixels before standardization to 5.661, 3.220, and 2.323 pixels in three iterations. For a better visualization, see the supplements for large frame-size movies of this experiment.

4.5 Quality of standardized images

We also visually inspected the image quality of an LNS pattern before and after our standardization process. Fig. 7 shows that all the local features of an image before standardization (Fig. 7 (a)(b)) were well preserved in the post-standardization image (Fig. 7 (c)(d)). No visible artifact was seen. The processed image was a little bit smoother, due to the interpolation process during the TPS warping. The overall loss of information was negligible.

4.6 Results of adult fruit fly VNC and others patterns

By modifying the shape prior of the principal skeleton, our algorithm can be easily adapted to other shape analysis applications. For example, in Fig. 1 (c) and (d) we show that the principal skeleton method can be used to standardize an adult fruit fly VNC. Indeed the adult VNC has a more complicated shape prior, which has 9 segments and 7 optimization domains (Fig. 8 (a)), than an LNS.

Similar to the LNS case, the key to standardizing an adult VNC is to detect the principal skeleton robustly. Fig. 8 (b) shows the results on 5 arbitrarily selected adult VNC patterns (data from J. Simpson lab; NC82 neuropile staining was used in place of N-cadherin). It is evident that our algorithm (upper row of Fig. 8 (b)) detected meaningful principal skeletons, while the image thinning (lower row, Fig. 8 (b)) produced results that were not very useful. Fig. 8 (c) and (d) show additional principal skeleton detection results of adult fruit fly center brain and *C. elegans*. It can be noted that even when the principal skeleton was poorly initialized to even outside the object in the *C. elegans* case (Fig. 8 (d)), our method still detected reasonable principal skeleton. Additional principal skeleton deformation movies can be found in the supplementary material.

One potential problem of our principal skeleton approach is that when a skeleton becomes more complicated, the deformation to the optimum may be more likely trapped into local minima. Generally speaking, this requires more careful initialization. One solution is to introduce hierarchical domains in optimization. Taking the adult VNC as an example, we can make our algorithm more robust by first optimizing the skeleton of the main trunk (i.e. the horizontal domain in Fig. 8 (a)) so that we can get a good estimation of the scale, position and the orientation of the VNC, and then optimizing the remaining domains/segments to complete the entire skeleton.

(a)
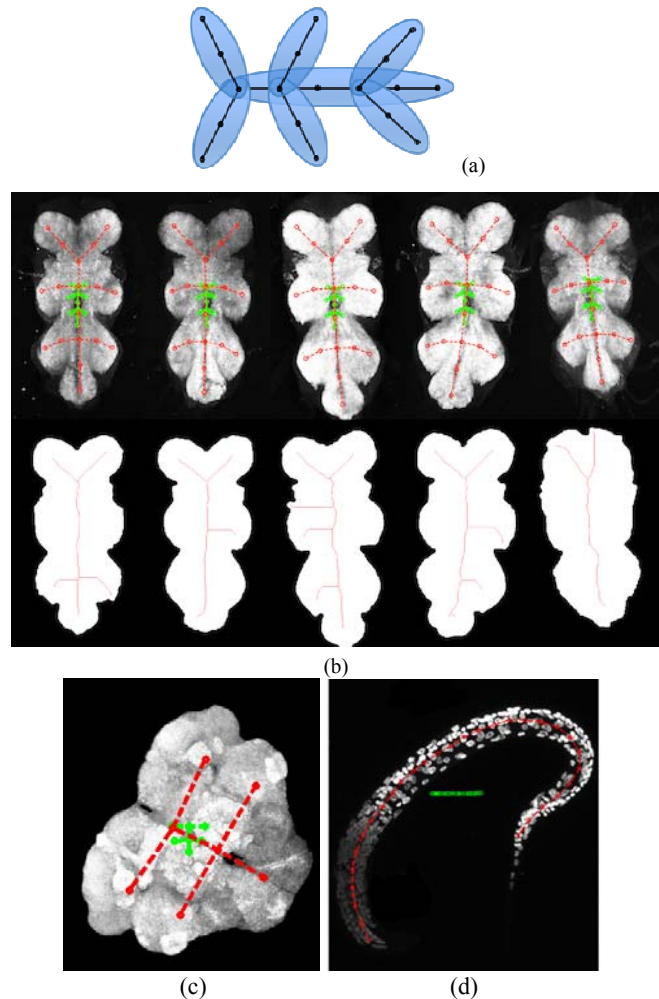

(b)

(c)   (d)

Fig. 8. (a) Shape prior of the adult VNC principal skeleton. (b) Results of principal skeleton detection (upper row) and thinning (lower row) on five adult VNC images (background image of the upper row). Green: initialization of the PS. Red: detected PS. (c) Principal skeleton detection of an adult fruit fly center brain. (d) Principal skeleton detection result of a *C. elegans* confocal image.

REFERENCES

Bookstein,F.L. (1989) Principal warps: thin-plate spline and the decomposition, *IEEE Transactions on Pattern Analysis and Machine Intelligence*, **11:** 567-585.

Brandt,J.W. *et al.* (1992) Continuous skeleton computation by Voronoi diagram. *CVGIP: Image Underst.*, **55(3)**:329-338.

Chuang,J.H. *et al.* (2004) A potential-based generalized cylinder representation. *Computer & Graphics*, **28(6)**:907-918.

Hastie,T. (1984) Principal curves and surfaces, Ph.D. Thesis Standford Univ.

Lam,L. *et al.* (1992) Thinning methodologies-a comprehensive survey, *IEEE Transactions on Pattern Analysis and Machine Intelligence*, **14(9):** 869-885.

Lein,E.S. *et al.* (2007) Genome-wide atlas of gene expression in the adult mouse brain. *Nature,* **445**:168–176.

Long,F., Peng,H., Liu,X. *et al.* (2009) A 3D digital atlas of *C. elegans* and its application to single-cell analyses. *Nature Methods,* **6(9)**: 667-672.

Malandain,G. *et al.* (1998) Euclidean skeleton. *Image and vision computing,* **16(5)**:317-327.

Peng,H., Long,F., Liu,X., Kim,S.K. and Myers,E.W. (2008) Straightening *C. elegans* images, *Bioinformatics*, **24**: 234-242.

Peng,H. (2008) Bioimage informatics: a new area of engineering biology. *Bioinformatics,* **24**: 1827-1836.

Peng,H. Ruan,Z, Long,F, Simpson,J.H., and Myers, E.W. (2010) V3D: a real-time 3d visualization system for the quantitative analysis of large bioimages and its applications to neuroscience. *Nature Biotechnology,* **28**. (In press)

Pfeiffer,B.D. *et al.* (2008) Tools for neuroanatomy and neurogenetics in *Drosophila. PNAS,* **105**: 9715-9720.

Rueckert,D. *et al.* (1999) Nonrigid registration using free-form deformations: application to breast MR images. *IEEE Trans. Medical Imaging,* **18**:712–721.

Sorzano,C.O.S., Thevenaz,P., Unser M. (2005) Elastic registration of biological images using vector-spline regulization. *IEEE Trans. Biomed. Eng.,* **52(4)**: 652-663.

Toga,A.W. (1999) *Brain Warping*. Academic Press, San Diego.